Chemical Science

ROYAL SOCIETY OF CHEMISTRY

EDGE ARTICLE

View Article Online
View Journal | View Issue

Cite this: *Chem. Sci.*, 2022, **13**, 10786

All publication charges for this article have been paid for by the Royal Society of Chemistry

The sequential structural transformation of a heptanuclear zinc cluster towards hierarchical porous carbon for supercapacitor applications†

Tian Li,[a] Yi-Fan Wang,[a] Zheng Yin,[c] Jian Li,[d] Xu Peng *[ad] and Ming-Hua Zeng *[ab]

The peripheral N/O chelating of Schiff base ligands, inner bridges, counterions, and metal centers gave rise to a brucite disk cluster $[Zn_7L_6(OCH_3)_6](NO_3)_2$ (**Zn_7**, (HL = 2-methoxy-6-((methylimino)-methyl)phenolate)) which crystallized into hexagonal prismatic plates. The combination of crystallographic studies, *in situ* TG-MS, and other characterization techniques showed that with a fixed metal and ligand composition in the precursors, weak correlative interactions (*e.g.*, electrostatic interactions) and shape matching between the cluster core and counterions determine the cluster packing modes in the crystals and affect their phase and morphological changes during pyrolysis. The tracking of the pyrolysis process showed that the peripheral ligands, inner bridge, and counterion decompose first, followed by the Zn_7O_6 core merging with cubic ZnO, which was then reduced by carbon and eventually evaporated, leaving behind a porous carbon structure. In this process, the solid material composition change was in the sequence {Zn_7}-{Zn–O core@C}-{ZnO@C}-{Zn@C}-{C}, which was accompanied by a porosity change from micropores to hierarchical pores, and then to micropores again. The core structure and packing modes of **Zn_7** evolved into micropores and mesopores, respectively. Micro-mesoporous carbon **Zn_7-1000** featured a capacitance of 1797 F g^{-1} at 1 A g^{-1}, where the BET specific surface area was 3119.18 m^2 g^{-1}, which, to the best of our knowledge, is the highest value reported for a porous carbon electrode. This work represents an important benchmark for the analysis of dynamic chemical processes involving coordination clusters at high temperatures, and it could lead to important applications in high-performance devices.

Received 18th July 2022
Accepted 19th August 2022

DOI: 10.1039/d2sc03987g

rsc.li/chemical-science

Introduction

Time-dependent evolutions of composite solid materials at elevated temperatures are highly complex processes that involve both chemical decomposition and condensation reactions. Understanding these processes by tracking the dynamic evolution of the solid-state material is both intriguing and challenging.[1] Usually, the entire pyrolysis reaction involves a synergistic effect applied to solid-state chemistry, including decomposition, agglomeration, carbonization and hydrocarbons by dry distillation.[2] However, these four processes are often interrelated and disordered, and it is difficult to find obvious and insightful rules, which significantly aggravates the analysis of the pyrolysis process. If the pyrolysis process can be controlled and idealized through the design of precursor molecules, for example, precursor templates, decomposition and ordering, quantification, and product porosity, it will greatly improve the efficiency of our analysis of the pyrolysis process. Designing multi-component materials at different levels that are used as precursors in controllable pyrolysis has successfully lead to various nanocomposite materials, especially functional carbon materials.[3] Some of these carbon materials have exceptional physical and chemical properties and can be used for energy storage and conversion devices, or as electrode materials for electrocatalysis.[4–6] However, designing hierarchical porous carbon materials with specific pore size distributions that are advantageous for specific applications remains both a challenge for material design and an opportunity for advancing the applications of these materials. Metal organic

[a]*Collaborative Innovation Center for Advanced Organic Chemical Materials Co-constructed by the Province and Ministry, Ministry-of-Education Key Laboratory for the Synthesis and Application of Organic Functional Molecules, College of Chemistry & Chemical Engineering, Hubei University, Wuhan, 430062, P. R. China. E-mail: pengxu@hubu.edu.cn*

[b]*Department of Chemistry and Pharmaceutical Sciences, Guangxi Normal University, Key Laboratory for the Chemistry and Molecular Engineering of Medicinal Resources, Guilin, 541004, P. R. China. E-mail: zmh@mailbox.gxnu.edu.cn*

[c]*College of Chemistry and Chemical Engineering, Shaanxi University of Science and Technology, Xi'an 710021, P. R. China*

[d]*AnHui Province Key Laboratory of Chemistry for Inorganic/Organic Hybrid Functionalized Materials, Anhui University, Hefei 230601, P. R. China*

† Electronic supplementary information (ESI) available. CCDC [2020712]. For ESI and crystallographic data in CIF or other electronic format see https://doi.org/10.1039/d2sc03987g

framework (MOF)-derived carbons inheriting the porous structure of the parent materials have been shown to have various pore distributions and high surface areas, and, thus, represent a promising route in this regard and its derivatives.[7–9] On the other hand, the controllable pyrolysis of predesigned coordinative molecular clusters is emerging as an effective new way of achieving carbon derivatives. However, derivation from non-porous coordinated molecular clusters to obtain hierarchical porous structures and high-performance carbon materials is a remarkable challenge. We, therefore, studied the solid–liquid and solid–solid structural correlation of self-assembled coordination clusters and elucidated the mechanism of their assembly, where significant effort was made in exploring simple solid-state transformations in the pyrolysis process. For example, by selecting two ligands with different shapes but similar coordination reactivities, we revealed the mechanism of competition and transformations between the different species in **Co$_4$**.[10] The rational introduction of a μ_3-CN inner bridge into **Co$_{7+1}$** clusters followed by pyrolysis created Co@NC core–shell nano materials that achieved a higher OER performance.[11] Also, the co-crystalline zinc clusters of **Zn$_{7+1+1}$** are completely pyrolyzed to a microporous carbon material with excellent capacitance performance.[12] The abovementioned studies provide a meticulous analysis of changes at the molecular and morphological level during the pyrolysis processes and constructs a preliminary structure–activity relationship between the coordination clusters and their derivatives, however, the sequential structural transformation has not yet been elucidated. In this report, we used elaborately designed multi-component precursors to systematically study the correlation between molecular level chemical reactions and solid material morphological changes in the thermolysis process. We employed a "molecule-to-condensed-matter" perspective in the design and characterization of the coordination clusters thermolysis reaction, where we established the time-dependent correlation between the material structures on molecular, cluster packing and crystal morphology levels.

Results and discussions

Based on the above understandings, a heptanuclear zinc cluster, $[Zn_7L_6(OCH_3)_6](NO_3)_2$ (**Zn$_7$**), was synthesized as hexagonal-prismatic-plate crystals from $Zn(NO_3)_2\cdot 6H_2O$ and the N/O chelated Schiff base ligand 2-methoxy-6-((methylimino)-methyl)phenolate in CH_3OH solution, where the μ_3-OCH_3 plays a crucial role for the formation of the heptanucleated cubic Zn–O core. The **Zn$_7$** disk cations are tightly arranged in layers parallel to the *ab* plane, which are then packed along the *c* axis. The NO_3^- counterions are located in the 1D channel formed by three adjacent columns of clusters. We use the zinc cluster **Zn$_7$** as the precursor, and the products after pyrolysis in an Ar atmosphere are designated as **Zn$_7$-*T*** (where *T* represent the annealing temperature). Notably, a carbon material with a micro-mesoporous hierarchical structure is carbonized at 1000 °C under an argon atmosphere (**Zn$_7$-1000**), presenting the highest Brunauer–Emmet–Teller (BET) specific surface area of 3119.18 $m^2\ g^{-1}$ and a pore volume of 1.82 $cm^3\ g^{-1}$, which exhibits excellent capacitance performance. The specific capacitance value is 1797 F g^{-1} when the current density reaches 1 A g^{-1}. We carried out a systematic analysis of the crystal structure of **Zn$_7$** and its evolution, which unravels the formation mechanism of the hierarchical porous carbon (Scheme 1).

X-ray single crystal diffraction analysis showed that **Zn$_7$** crystallized in the trigonal system $P\bar{3}c1$ space group. It is composed of a $[Zn_7L_6(OCH_3)_6]^{2+}$ cation cluster and two counter anions of NO_3^- but without any lattice solvents, indicating highly condensed packing (Fig. S2a and Table S1a†). The peripheral Schiff base ligands adopting a η_1:η_2:η_1:μ_2 coordination and six μ_3-OCH_3 as inner bridges grasp seven Zn^{2+} ions in to a cluster with a disk core. All Zn^{II} atoms are in a six-coordinated octahedral configuration, with the central ZnO_6 octahedron surrounded by six outer $ZnNO_5$ octahedrons. The core of the disk is similar to brucite-like fragments and all seven Zn^{2+} ions are located in a coplanar fashion, with a Zn–OCH_3 bond length of 2.036 to 2.127 Å, and a Zn–O–Zn angle of 94.6–101.3°. The benzene ring based peripheral ligands endow the cluster duple open hemispheres at two sides of the disk. Three inner –OCH_3– motifs coordinate vertically to the **Zn$_7$** plane, which sit inside the bowl and occupy the void space that could potentially host solvent molecules. As a result, weak intermolecular interactions induce a cluster packing mode, where eight **Zn$_7$** disks are located at the vertex of a quadrilateral prism with four additional disks at the middle position of the pillar. Two 1D channels with triangular windows are generated in each cell to host the NO_3^-. The regular vertical arrangement of the disk with duple open hemispheres and the hydrophobic –OCH_3– sitting inside the bowl facilitates the close packing of the heptanuclear cations and the facile removal of NO_3^- trapped in the 1D inter-cluster channel during pyrolysis. The nearest inter-cluster distance is 11.64 and 14.12 Å along the plane and vertical direction, respectively, considering the center Zn···Zn distance for adjacent disks (Fig. S2c†).

The simulation of the crystal morphology of **Zn$_7$** using the Bravais–Friedel–Donnay–Harker (BFDH) method showed a hexagonal prism-shaped morphology (Fig. S3†),[13] which was

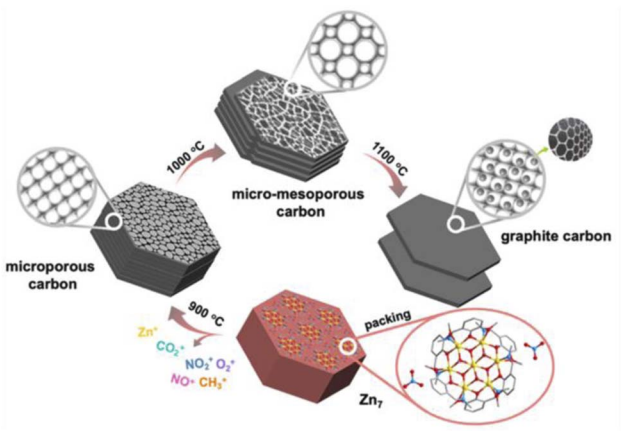

Scheme 1 Progressive phase transformation from a heptanuclear zinc cluster (**Zn$_7$**) to hierarchical porous carbon (**Zn$_7$-1000**). The microporous carbon samples **Zn$_7$-900** and **Zn$_7$-1100** are also illustrated.

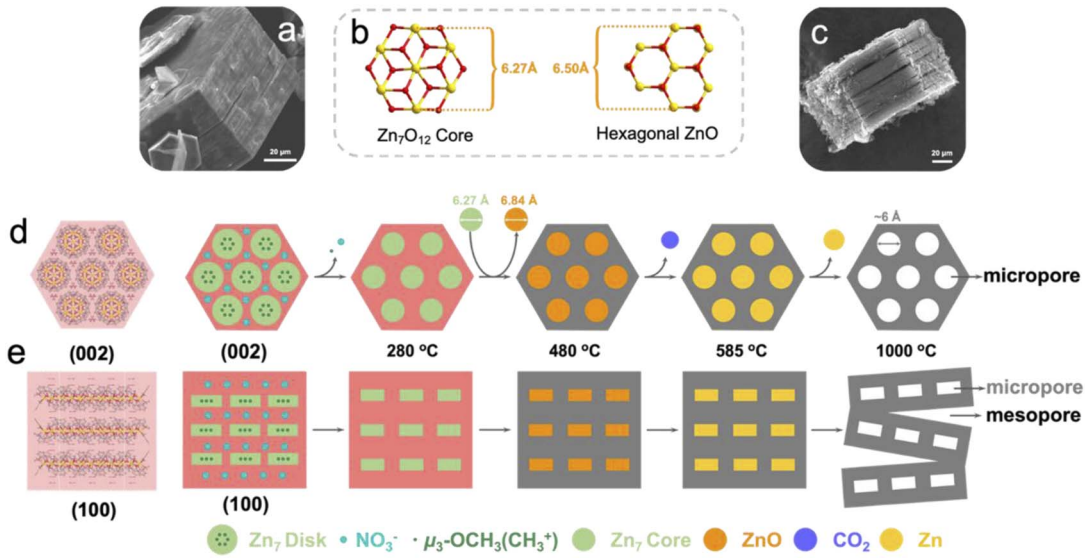

Fig. 1 Stacking structure analysis to explain the mechanism for the generation of micropores and mesopores formed in the pyrolysis products. (a) An SEM image of Zn_7. (b) Crystallization process from the Zn_7 core to hexagonal ZnO. (c) An SEM image of Zn_7-1000. The pyrolysis mechanism of Zn_7, with the observation direction along (d) the (002) plane and (e) the (100) plane.

consistent with that of the obtained sample (Fig. 1a). The [Zn_7] units parallel the hexagonal plane of the crystal, and the NO_3^- anions sit above and below the individual heptanuclear complexes, which interact with the ligand of the Zn_7 cluster through C–H···O hydrogen bonding interactions. When the observing direction is along the (002) plane and the (100) plane, the surface where the nitrate is located is parallel to the (002) surface while being perpendicular to the (100) surface of $[Zn_7L_6(OCH_3)_6]^{2+}$ (Fig. S3d–f†). For such hexagonal prism crystals constituting the disks arranged in a compact manner, the horizontal and vertical intercluster interactions contribute to the maintenance of the hexagonal morphology during the high temperature carbonization process. When the pyrolysis temperature is 1000 °C, the crystal still maintains a hexagonal prism shape, but shows a slit when viewed from the side of the crystal; slits can be observed parallel to the *ab* plane (Fig. 1c). This macroscopic observation is strongly related to the thermal decomposition of microscopic molecules.

In the first stage of decomposition (205–280 °C), CH_3^+, NO^+, NO_2^+, O_2^+ fragments are detected by TG-MS (Fig. 2b). Among them, the methyl group is attributed to the cracking of μ_3-OCH_3 and the methoxy group of L, which with the C–O bond in Zn_7 of similar strength (Table S1b†) and the O_2^+ is ascribed to the decomposition of nitrate and its further reactions ($2NO_3^- = 2NO_2 + O_2$, $NO_2 + C = 2NO + CO_2$) (Table S2†). It should be noted that the first stage of decomposition is completed at 280 °C, where Zn_7 collapses to form an amorphous structure, yet the Zn_7 core still remains independent (Fig. S4a†). At the same time, due to the removal of nitrate "planes", the force between the "planes" where the Zn_7 core is located is significantly reduced, and a tendency to separate would start to develop. A heptanuclear $[Zn_7O_{12}]$ core with a diameter of about 6.27 Å transform into hexagonal ZnO with a diameter of about 6.50 Å in the temperature range of 280–480 °C (Fig. S4a†). In this process, the

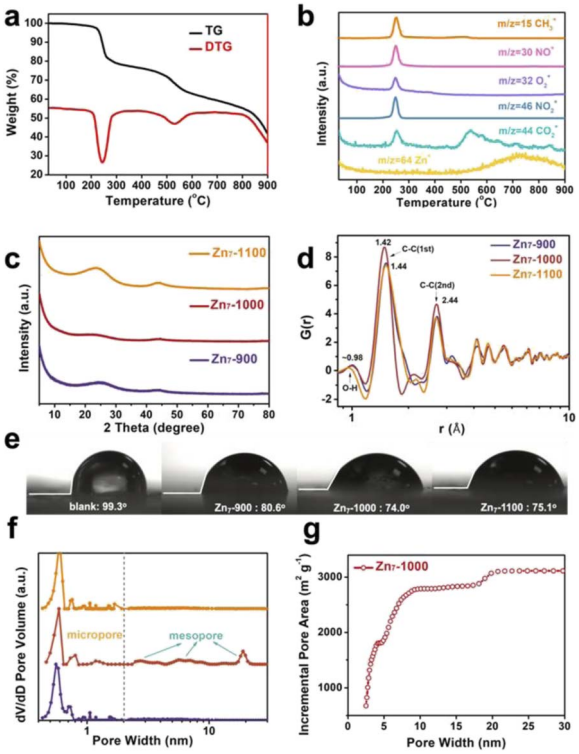

Fig. 2 Physical property analysis. (a) TG and DTG curves of Zn_7. (b) Evolution profiles of the main gaseous decomposition products (*m*/*z* 15, methane; *m*/*z* 30, nitric oxide; *m*/*z* 32, oxygen; *m*/*z* 46, nitrogen dioxide; *m*/*z* 44, carbon dioxide; *m*/*z* 64, zinc) derived from Zn_7 pyrolysis process tracking *via* TG-MS. (c) Powder XRD patterns, (d) PDF analysis, and (e) static contact angles of **blank**, Zn_7-900, Zn_7-1000, and Zn_7-1100 samples. Pore structure analysis. (f) Pore size distributions calculated from N_2 adsorption isotherms for Zn_7-900, Zn_7-1000, and Zn_7-1100. (g) Relationship between the cumulative pore area and the pore diameter of Zn_7-1000.

elaborately designed cluster with a precise spatial arrangement of ligands, counterions and the Zn_7 core enables the coherent decomposition and departure of the nitrate group with methoxy species, which helps to maintain the regular morphology and ordered mesoscopic structure of the resulting ZnO@carbon structure. In the second stage (480–585 °C), the primary chemical reaction is $7ZnO + 7/2C = 7Zn + 7/2CO_2$ (Table S3†). The stoichiometric number 7 is due to the fact that there are seven Zn atoms in a Zn_7 molecule. In the third stage of decomposition (>585 °C), Zn^+ is detected by TG-MS because the liquid zinc element began to evaporate and escape (Fig. 2b), and left micropores with a diameter of about 6 Å at 900 °C (Fig. 1d). Moreover, at 1000 °C, the abovementioned separation between the "planes" where the Zn_7 cores are located results in a large number of slit-type mesopores at 1000 °C (Fig. 1e).[14] In brief, inorganic metal nodes in molecular clusters can be converted into metal oxides by pyrolysis, and further reduced to elemental metals by a carbothermal reduction process, while Zn molecular clusters can generate pore structures of specific sizes in pyrolyzed carbon-based materials during this process. The phase evolution process can be summarized as $Zn_7[C_6H_3(CH_3O)(O)(NCH_3)]_6$ $(OCH_3)_6(NO_3)_2$ → $[Zn_7O_{12}]$@N,O-doped carbon → [ZnO]@N,O-doped carbon → [Zn]@N,O-doped carbon → N,O-doped hierarchical carbon. Obviously, choosing clusters with specific morphologies for pyrolysis can further change the pore structure of the pyrolysis products and increase the porosity of the derived carbon materials.

A series of characterizations, including PXRD, *ex situ* SAXS, PDF, TEM, Raman and BET were conducted to further illustrate the thermal decomposition process of Zn_7 and the pore structure changes during pyrolysis. The PXRD patterns of 280–480 °C pyrolysis samples show a clear hexagonal ZnO peak (JCPDS card 65-3411), indicating that the Zn_7 core is crystallized into hexagonal ZnO. Meanwhile, the PXRD patterns of 600–800 °C pyrolysis samples also exhibit a strong diffraction peak of ZnO, which is derived from the remaining elemental zinc in the samples oxidized by oxygen in air after the annealing process (Fig. S4†). It should be noted that the PXRD pattern of the **Zn_7-900** sample has a broad and diffuse diffraction peak near $2\theta = 23°$ and a weak diffraction peak near $2\theta = 44°$, which is a distinct characteristic of amorphous carbon.[15] Also, among the diffraction peak at $2\theta = 23°$, the diffraction peak of **Zn_7-1000** is the weakest, which indicates that the degree of graphitization is the lowest ($R = 1.36$), while the diffraction peak of **Zn_7-1100** is narrowed to a certain extent, demonstrating an increased degree of graphitization ($R = 2.19$).[16] Furthermore, experimental atomic pair distribution function (PDF) analysis also proves that the peak is centered at 1.42 Å of **Zn_7-1000** (slightly smaller than other samples, ~1.44 Å) corresponding to the sp^2 C–C bond in graphitic carbon, which is also consistent with the sequential phase evolution process deduced by TG-MS and other structural characterization[17] (Fig. 2c and d). *Ex situ* SAXS patterns of **Zn_7-900**, **Zn_7-1000**, and **Zn_7-1100** are shown in Fig. S5.† In addition, high-resolution transmission electron microscopy (HRTEM) mapping displays the disordered carbon layer in **Zn_7-900** and **Zn_7-1000** samples, while **Zn_7-1100** contains lattice fringes corresponding to graphitic carbon (002), indicating that amorphous carbon has crystallized into graphitic carbon (Fig. S6†). Similarly, in Raman spectra, the I_D/I_G value of the pyrolysis products (T = 900, 1000, 1100 °C) remained approximately the same, with an intensity ratio of 0.94, essentially indicating no apparent changes in the degree of carbon defects in the resulting material (Fig. S7†). ICP data of the Zn residual within the sample is shown in Table S4.† According to the analysis of the XPS spectrum, there are predominantly noticeable peaks of C and O elements in the sample (Fig. S8–S10†). The presence of the element O confirms that the surface of the material has oxygen-containing functional groups, which can enhance the hydrophilicity of the surface of the material to the water-based electrolyte and encourage the transfer of electrolyte ions; it can also introduce certain Faraday pseudo capacitors to enhance the capacitor performance.[27] The presence of hydrophilic functional groups can also be verified from the PDF data, where a peak at 0.98 Å is ascribed to the considerable O–H bond distance in the sample. Therefore, we used the polyurethane mixed sample and coated the film to conduct the contact angle test. In comparison with the blank, the contact angles of the three samples after high-temperature pyrolysis are $\theta < 90°$, and they all show hydrophilicity. Among them, the contact angle of **Zn_7-1000** is the smallest, indicating that better hydrophilic characteristics are more conducive to the contact between the ions in the electrolyte solution and the material (Fig. 2e).

In the gas adsorption measurements, a high gas uptake at a low pressure range corresponds to the presence of micropores and the hysteresis loop suggests mesoporous adsorption (Fig. S12†). The 900 °C pyrolysis product has microporous vacancies left by the evaporation and escape of zinc, with a pore size of about 0.6 nm.[12,18] In addition, there are other micropores that provide more adsorption sites during energy storage (Fig. 2f).[19–22] After being carbonized at a high temperature of 1000 °C, the pore size distribution shows that the **Zn_7-1000** sample contains mesopores, making the product show a micro-mesoporous hierarchical structure. These pores can become channels for the diffusion of electrolyte ions and accelerating ionization. The diffusion and transfer are rapid, and the surface area utilization rate has significantly improved. Compared with **Zn_7-900** and **Zn_7-1100**, the adsorption capacity of **Zn_7-1000** is significantly increased to 1295.16 $cm^3\ g^{-1}$ (Fig. S12b†) with a more significant proportion of mesopores. Calculation results of the density functional theory (DFT) method[23–25] show that the pore structure of **Zn_7-1000** primarily consists of pore sizes of 0.6 nm, 0.8 nm, ~1.2 nm, 3–8 nm, and 20 nm, of which 20 nm is attributed to the gap between the crystal blocks (Fig. 2f). **Zn_7-1000** has a maximum BET specific surface area, as high as 3119.18 $m^2\ g^{-1}$, and a maximum total pore volume of 1.82 $cm^3\ g^{-1}$ (Fig. S12d†). According to the curve of the cumulative specific surface area with the pore diameter calculated by the NLDFT method, it can be seen that the increase of the **Zn_7-1000** specific surface area is mainly due to the contribution of mesopores (Fig. 2g). The ultra-high specific surface area of **Zn_7-1000** and the extensive micropore–mesoporous hierarchical structure can facilitate more electrolyte ion adsorption sites.[26] Briefly, we have discovered the distinct characteristics of **Zn_7-1000** and

other pyrolyzed samples, and these differences are destined to have a significant impact on its electrochemical performance.

Compared with **Zn_7-900** and **Zn_7-1100**, which only have a single micropore size, **Zn_7-1000** combines micropores and mesopores to form a hierarchical porous structure that uses not only mesopores to provide efficient diffusion channels, but also micropores or smaller mesopores that leads to a larger active area, thereby achieving a high capacitance in supercapacitors. In order to verify our above analysis of the pyrolyzed samples from the zinc cluster on the electrochemical performance, we determined their specific capacitance by cyclic voltammetry (CV), galvanostatic charge and discharge (GCD) and electrochemical impedance spectroscopy (EIS) measurements, using a three-electrode configuration with Ag/AgCl as the reference electrode. The CV curves of **Zn_7-900**, **Zn_7-1000**, and **Zn_7-1100** samples range from −0.6 to 1.0 V at a scan rate of 5 to 100 mV s^{-1}. The shape of the CV curves under different scanning rates is not ideally rectangular-like; a prominent redox peak is especially located at *ca.* 0.3–0.4 V. This phenomenon indicates that a C=O group exists in the pyrolyzed samples, which is consistent with XPS analyses.[27] In addition, the slight difference in the position of the redox peak is due to the difference in the content of the pyridine nitrogen and the pyrrole nitrogen in the resulting materials (Fig. 4b, S11 and S13†).[28]

Moreover, GCD curves of **Zn_7-1000** electrode were tested, as shown in Fig. 3b and S14,† and exhibit a specific capacitance of 1797, 1473, 1297, 1113, and 877 F g^{-1} at current densities of 1, 2, 5, 10, and 20 A g^{-1}, respectively. This value records the best value among porous carbons as electrodes from MOFs or MOFs-derived materials as precursors (Fig. 4d and Table S5†). Also, the electrochemical impedance spectroscopy test was performed using a three-electrode configuration from 100 kHz to 100 mHz (Fig. 3c). A relatively low equivalent series resistance of only 10.71 Ω is exhibited by **Zn_7-1000**, reflected at the high-frequency region by the intersection of the curve at the real part. Meanwhile, the slope of **Zn_7-1000** is also larger than that of **Zn_7-900** and **Zn_7-1100**, revealing a better transport and diffusion of ions in **Zn_7-1000** samples (Fig. 3d). **Zn_7-1000** still has a superior specific capacitance retention compared with other samples under a current density of 2 A g^{-1} to 20 A g^{-1}, which is due to the reduced ion transfer resistance assisted by its microporous–mesoporous hierarchical structure.

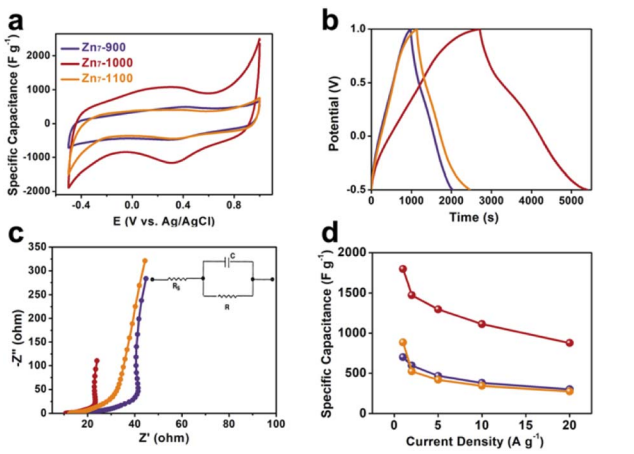

Fig. 3 Supercapacitive performance of **Zn_7-*T*s**. (a) A comparison of the CV curves at 5 mV s^{-1}. (b) A comparison of the GCD curves at a current density of 1 A g^{-1}. (c) A comparison of the electrochemical impedance spectroscopy (EIS) data. (d) A comparison of the specific capacitance values of **Zn_7-900**, **Zn_7-1000**, and **Zn_7-1100**.

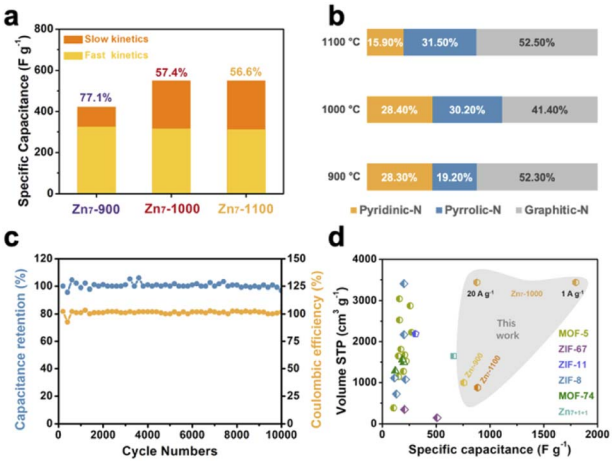

Fig. 4 Supercapacitive behavior analysis of **Zn_7-*T*s**. (a) Histograms of the capacitance contributions in the different samples, where orange represents fast kinetic processes and yellow represents slow kinetic processes. The percentage values represent the contribution of fast-kinetics capacitance to the overall capacitance ratio at 100 mV s^{-1}. (b) The proportion of C, N, and O elements in **Zn_7-*T*s**. (c) Capacitance retention and coulombic efficiency of **Zn_7-1000** over 10 000 charge/discharge cycles. (d) A comparison of our carbon material (**Zn_7-*T*s**) with related reports in the literature.

Conclusions

In summary, a heptanuclear zinc disk, **Zn_7**, was rational designed *via* a judicious choice of peripheral N/O-chelating Schiff base ligands, inner bridges, counteracting ions, and metal centers, where a predesigned ligand and metal ion ratio, weak interactions, and shape matching have been dominant in determining the cluster structure and packing mode. The structure and chemical composition of **Zn_7** were studied *via* TG-MS, which showed that pyrolysis leads to a sequential structural transformation that turns from crystal to MO/M@C and then to carbon. The study elucidated the formation mechanism of

pores, both in terms of the decomposition–condensation reaction mechanism and the cooperative bonding and packing in the cluster structure. This is, thus, the first time that the effects of the main ligand, inner bridge, and counterions on the formation, morphology, packing, and decomposition of coordination clusters have been thoroughly studied. It was noted that the precisely arranged cluster core, counterion ligands, hierarchical bonds in the crystal, and sequential derivative as a function of temperature and time lead to a coherent decomposition and departure of species and a structural transformation into an ordered porous structure. **Zn_7-1000** with a hierarchical pore structure exhibits excellent supercapacitor performance with a capacitance of 1797 F g^{-1} at 1 A g^{-1}, which, to the best of our knowledge, corresponds to the best value among reported porous carbon electrodes. To summarize, we established a new route to study the complex pyrolysis reaction of coordination clusters, which could inspire the rational design of functional nanomaterials from coordination compounds. We have provided a new vision for condensed matter chemistry, based on molecular, cluster packing, and crystal morphology levels, that unravels time-dependent changes in a high-temperature solid-state reaction and the relationship with the material properties.

Data availability

All experimental data associated with this article have been included in the main text and ESI.†

Author contributions

Xu Peng and Ming-Hua Zeng conceived the idea, co-wrote the paper and supervised the whole experimental procedure and data analysis. Tian Li, Yi-Fan Wang, Zheng Yin and Jian Li performed the experiments, analyzed the data and wrote the manuscript. All the authors discussed the results, commented on and revised the manuscript.

Conflicts of interest

There are no conflicts to declare.

Acknowledgements

This work was financially supported by the NSFC (Grants 22171075), the NSFC of Hubei (Grants 2021CFB420), and the BAGUI talent program (2019AC26001).

Notes and references

1 Y. Jia, Z. Xue, J. Yang, Q. Liu, J. Xian, Y. Zhong, Y. Sun, X. Zhang, Q. Liu, D. Yao and G. Li, *Angew. Chem., Int. Ed.*, 2022, **61**, e202110838.
2 P. Basu, in *Biomass Gasification Design Handbook*, Elsevier, 2010, pp. 65–96.
3 Y.-Z. Chen, C. Wang, Z.-Y. Wu, Y. Xiong, Q. Xu, S.-H. Yu and H.-L. Jiang, *Adv. Mater.*, 2015, **27**, 5010–5016.
4 H. Shao, Y.-C. Wu, Z. Lin, P.-L. Taberna and P. Simon, *Chem. Soc. Rev.*, 2020, **49**, 3005–3039.
5 Y.-S. Hu, P. Adelhelm, B. M. Smarsly, S. Hore, M. Antonietti and J. Maier, *Adv. Funct. Mater.*, 2007, **17**, 1873–1878.
6 W. Tian, H. Zhang, X. Duan, H. Sun, G. Shao and S. Wang, *Adv. Funct. Mater.*, 2020, **30**, 1909265.
7 J. Hou, C. Cao, F. Idrees and X. Ma, *ACS Nano*, 2015, **9**, 2556–2564.
8 S. Dutta, A. Bhaumik and K. C.-W. Wu, *Energy Environ. Sci.*, 2014, **7**, 3574–3592.
9 B. Fang, J. H. Kim, M.-S. Kim and J.-S. Yu, *Acc. Chem. Res.*, 2013, **46**, 1397–1406.
10 H.-L. Zheng, X.-L. Chen, T. Li, Z. Yin, Y. Zhang, M. Kurmoo and M.-H. Zeng, *Chem.–Eur. J.*, 2018, **24**, 7906–7912.
11 J.-Q. Zhao, D. Cai, J. Dai, M. Kurmoo, X. Peng and M.-H. Zeng, *Sci. Bull.*, 2019, **64**, 1667–1674.
12 Y. Wang, Y. Liang, Y. Wu, J. Yang, X. Zhang, D. Cai, X. Peng, M. Kurmoo and M. Zeng, *Angew. Chem., Int. Ed.*, 2020, **59**, 13232–13237.
13 R. Docherty, G. Clydesdale, K. J. Roberts and P. Bennema, *J. Phys. D: Appl. Phys.*, 1991, **24**, 89–99.
14 Z. Li, W. Lv, C. Zhang, B. Li, F. Kang and Q.-H. Yang, *Carbon*, 2015, **92**, 11–14.
15 B. Liu, H. Shioyama, T. Akita and Q. Xu, *J. Am. Chem. Soc.*, 2008, **130**, 5390–5391.
16 Y. Liu, J. S. Xue, T. Zheng and J. R. Dahn, *Carbon*, 1996, **34**, 193–200.
17 V. Petkov, Y. Ren, S. Kabekkodu and D. Murphy, *Phys. Chem. Chem. Phys.*, 2013, **15**, 8544.
18 M. J. Wang, Z. X. Mao, L. Liu, L. Peng, N. Yang, J. Deng, W. Ding, J. Li and Z. Wei, *Small*, 2018, **14**, 1804183.
19 J. Chmiola, *Science*, 2006, **313**, 1760–1763.
20 J. Chmiola, C. Largeot, P.-L. Taberna, P. Simon and Y. Gogotsi, *Angew. Chem.*, 2008, **120**, 3440–3443.
21 D. T. L. Galhena, B. C. Bayer, S. Hofmann and G. A. J. Amaratunga, *ACS Nano*, 2016, **10**, 747–754.
22 E. Raymundo-Piñero, K. Kierzek, J. Machnikowski and F. Béguin, *Carbon*, 2006, **44**, 2498–2507.
23 M. Thommes and K. A. Cychosz, *Adsorption*, 2014, **20**, 233–250.
24 M. Thommes, K. Kaneko, A. V. Neimark, J. P. Olivier, F. Rodriguez-Reinoso, J. Rouquerol and K. S. W. Sing, *Pure Appl. Chem.*, 2015, **87**, 1051–1069.
25 A. V. Neimark, Y. Lin, P. I. Ravikovitch and M. Thommes, *Carbon*, 2009, **47**, 1617–1628.
26 P. Hao, Z. Zhao, J. Tian, H. Li, Y. Sang, G. Yu, H. Cai, H. Liu, C. P. Wong and A. Umar, *Nanoscale*, 2014, **6**, 12120–12129.
27 H. A. Andreas and B. E. Conway, *Electrochim. Acta*, 2006, **51**, 6510–6520.
28 T. Lin, I.-W. Chen, F. Liu, C. Yang, H. Bi, F. Xu and F. Huang, *Science*, 2015, **350**, 1508–1513.
29 H.-S. Kim, J. B. Cook, H. Lin, J. S. Ko, S. H. Tolbert, V. Ozolins and B. Dunn, *Nat. Mater.*, 2017, **16**, 454–460.
30 C. Choi, D. S. Ashby, D. M. Butts, R. H. DeBlock, Q. Wei, J. Lau and B. Dunn, *Nat. Rev. Mater.*, 2020, **5**, 5–19.